Project Acronym:

BRAINSONIC (ENTERPRISES/0223/Sub-Call1/0057)

MRI-guided Focused Ultrasound robotic system for brain tumors.

Deliverable number: 4.1

Title: Development of phantom with tumor mimics.

Prepared by:

Leonidas Georgiou (LINAC)
Antonis Christofi (LINAC)
Antreas Chrysanthou (LINAC)
Christakis Damianou (CUT)

Date: 20/01/2025

Funded by the European Union NextGenerationEU
Cyprus tomorrow RECOVERY AND RESILIENCE PLAN
Republic of Cyprus
RESEARCH & INNOVATION FOUNDATION

The BRAINSONIC project is funded by the Recovery and Resilience Facility of the NextGenerationEU instrument, through the Research and Innovation Foundation (RIF) of Cyprus.

Contents

EXECUTIVE SUMMARY

This deliverable presents the methodologies employed and key results obtained in the process of developing a high-quality tumor-bearing brain/skull phantom, which will serve as a pivotal tool for assessing the BRAINSONIC therapeutic system and protocol. Preliminary results of phantom sonications in the MRI setting were included as a proof of concept.

Our initial objective was to develop and characterize various agar/silica phantoms to explore how different concentrations of inclusions impact their key properties. For this purpose, the thermal (thermal conductivity, thermal diffusivity, and specific heat capacity), acoustic (propagation speed, acoustic impedance, and attenuation coefficient), and Magnetic Resonance Imaging (MRI) relaxation properties of seven phantoms developed with either different agar concentration or a constant amount of agar and varying silica concentration were investigated.

Our assessment was then focused on the phantoms' ability to generate ablative temperatures and manifest thermal lesions on post-sonication MR images. The study specifically examined the impact of agar and silica concentrations on the focal temperatures generated by high-power sonications within the phantoms, utilizing MR thermometry inside a 3T MRI scanner. Following sonication, high-resolution coronal and axial images were acquired to assess lesion visibility and contrast with the surrounding unheated area, as well as to monitor lesion regression over time.

Following preliminary experiments to evaluate the key properties and heating capacity of phantoms with varying agar and silica concentrations, we developed the tumor-bearing head phantom. This phantom consists of a 3D printed skull mimic filled with a tissue-mimicking agar gel, further including an embedded silica-doped tumor mimic. The agar/silica composition for the brain tissue and tumor-mimicking materials was chosen based on our preliminary assessment outcomes, primarily to achieve the desired contrast and differentiate the thermal response between the tumor and its surrounding tissue. The skull mimic was developed as a two-compartment structure, which includes a removable circular insert. This design enables the incorporation of skull inserts made from various thermoplastic materials and facilitates sonications both through the skull insert and in free field conditions.

Finally, the developed tumor-bearing brain/skull phantom underwent MRI evaluation, serving a dual purpose: firstly, to examine the overall MRI characteristics of the phantom and tumor visibility; and secondly, to measure focal temperatures and accumulated thermal dose resulting from high-power sonications within the tumor simulator in free field and through different thermoplastic skull inserts, with the ultimate goal to demonstrate its suitability for its intended application in brain MRI-guided Focused Ultrasound (MRgFUS).

INTRODUCTION

Gliomas are brain tumors graded from I to IV based on their growth rate. Median survival rates range from 5 to 15 years for low-grade gliomas and 9 to 12 months for high-grade ones. Glioblastoma multiforme (GBM) is a grade IV tumor, known for its aggressive nature and high fatality rate. Even with multimodal therapies, such as surgery combined with radiation and/or chemotherapy, the prognosis for GBM patients remains bleak, with a median survival time of merely 12 months [1-3].

Macroscopically, GBMs primarily manifest within the cerebral hemispheres, predominantly in the supratentorial white matter. They typically lack distinct margins and instead present as diffusely infiltrating masses [4]. They vary in texture and appearance. Some are solid and white, some soft and yellow due to dying tissue, and others are cystic with bleeding. Furthermore, they typically exhibit non-uniform growth patterns along the white matter and occasionally along the periphery of cerebrospinal fluid-filled areas. As a consequence, the shapes of resulting tumors are irregular and vary significantly among individuals [5,6].

Magnetic resonance imaging (MRI) serves as the main diagnostic method for GBM [7], providing essential clinical information through basic sequences, such as T1- and T2-weighted [8]. More advanced techniques, such as multi-parametric MRI, are increasingly utilized for a more comprehensive assessment of GBM features and characteristics [8]. Interestingly, when GBM affects the corpus callosum, it often presents a distinct butterfly-shaped pattern on the MRI scans, indicating involvement of bilateral occipital and temporal lobes [9].

GBMs exhibit a wide variation in their size, spanning from few centimetres to extremely large tumors replacing the whole hemisphere, while infiltration extends beyond the visible edges of the tumor in all cases [4]. For instance, tumors exceeding 8 cm might extend beyond the midline or occupy about half of the hemisphere [10]. Typically, GBMs have already grown to several cm in size by the time of diagnosis, although specific findings vary significantly across different studies.

According to Ulutin et al. [7] the tumor diameter upon diagnosis is typically around 4 cm. A similar conclusion was reached in another study involving 19 patients with an average age of about 67 years, where T1-imaging revealed an average tumor size of about 4.2 cm [11]. In a study conducted by Simpson et al. [12], involving 645 patients, it was found that 38% of the patients had a tumor diameter of less than 5 cm, 56% fell within the range of 5–10 cm, and 6% of patients presented with tumors larger than 10 cm at the time of diagnosis. For pediatric glioblastoma [13], the mean tumor size, as determined on axial CT scans, was approximately 5.8 cm, ranging from a minimum of 2 cm to a maximum of 9.3 cm. Notably, authors in [10] classified tumors smaller than 4 cm as small-sized, while those equal to or larger than 6 cm were deemed large.

It is also interesting to mention the study of Curtin et al. [14], who examined lacunarity and fractal dimension metrics of GBMs on MRI images and whether they are linked to patient survival. The study outcomes showed a significant association of the shape of abnormalities seen on T2-weighted and fluid attenuated inversion recovery (FLAIR) MRI with survival.

Tissue mimicking phantoms (TMPs) are designed to replicate essential human tissue properties, enabling the assessment of imaging and treatment techniques before their use in live subjects. Creating GBM phantoms presents a very challenging task due to the intricate tumor growth patterns and wide variability in tumor properties, size and shape among individuals. A physical head and neck model, including a GBM simulator, dedicated to simulating brain disorders in radiology and radiotherapy studies has been developed by the Ionizing Radiation Research Group (NRI) [15,16]. However, to the best of our knowledge no tumor bearing head phantoms (replicating both brain tissue and skull) specifically designed for FUS applications exist in previous literature.

1. MATERIALS AND METHODS

1.1 Development of phantoms with different agar/silica concentrations

Seven (7) different phantoms were prepared using agar (Merck KGaA, Darmstadt, Germany) as the gelling agent. Phantoms with 2, 4 and 6 % weight per volume (w/v) agar concentration were prepared. Phantoms containing a constant amount of 6 % w/v agar and increasing amount of silicon dioxide (Sigma-Aldrich, Missouri, USA); referred to as silica for simplicity, of 2, 4, 6, and 8 % w/v were prepared as well. **Figure 1** displays photos of the developed phantoms, indicating the concentration of agar and silica in each.

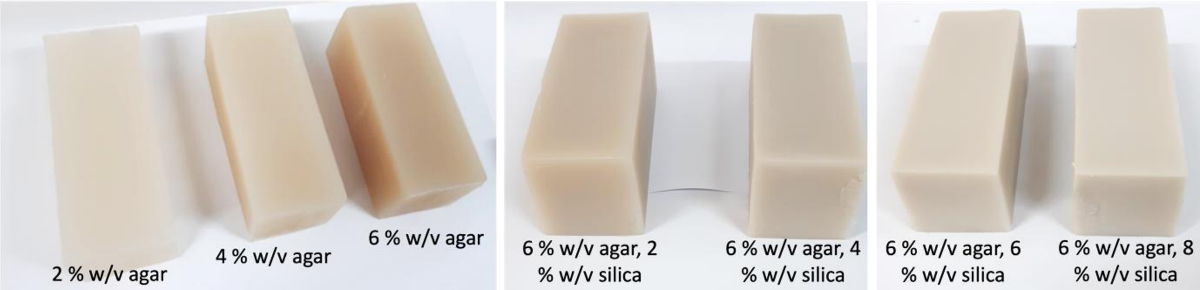

Figure 1: *Photos of the developed phantoms with varied concentrations of agar and silica.*

For each experiment described below, the phantoms were prepared a day in advance using specially designed 3D-printed Polylactic Acid (PLA) molds (CR-10, Creality, Shenzhen, China), tailored to the specific setup requirements of each experiment. The process for creating the gel phantom, as previously outlined by Drakos et al. [17], involved dissolving the agar and silicon dioxide powders in water. The phantoms were allowed to solidify overnight at room temperature and then removed from the molds the following morning.

1.2 Characterization of agar/silica phantoms

1.2.1 Density

The density of each phantom (ρ) was determined by calculating the ratio of its mass to volume. The mass of each phantom was measured with a high-precision digital scale (1479V, Tanita Corporation, Tokyo, Japan) while the volume was measured by immersing the tested sample in a volumetric tube filled with water and employing the water displacement method.

1.2.2 Acoustical properties

For experimental measurement of the acoustic properties (propagation speed, acoustic impedance, and attenuation coefficient), the various phantoms were developed in specially designed PLA molds with dimensions of 2.6 cm (width) × 3.2 cm (length) × 4 cm (height), as shown in the indicative photo of **Figure 2A**.

Ultrasonic propagation speed

The ultrasonic propagation speed in each phantom was measured using the pulse-echo method. The planar transmitter transducer and each phantom were accommodated at specific locations on a 3D-printed holder with an aluminium plate mounted close to the back surface of the phantom serving as a reflector, and everything submerged in a tank filled with degassed/deionised water. The transducer was connected to the pulser/receiver (500 PR, GE Panametrics, 221 Crescent St., Waltham, MA 02453, USA, 25 MHz bandwidth) that was in turn connected to the oscilloscope (TDS 2012, Tektronix, Inc., 14150 SW Karl Braun Drive, USA). Measurements were conducted utilizing both a 2.2 MHz transducer (diameter of 10 mm, in-house, element from QX Ultrasonic, Beijing, China) and 2.7 MHz transducer (diameter of

10 mm, Piezo Technologies, Indianapolis, USA), both serving as transmit/receive transducers. **Figure 2B** illustrates the experimental set-up utilized for measuring the propagation speed.

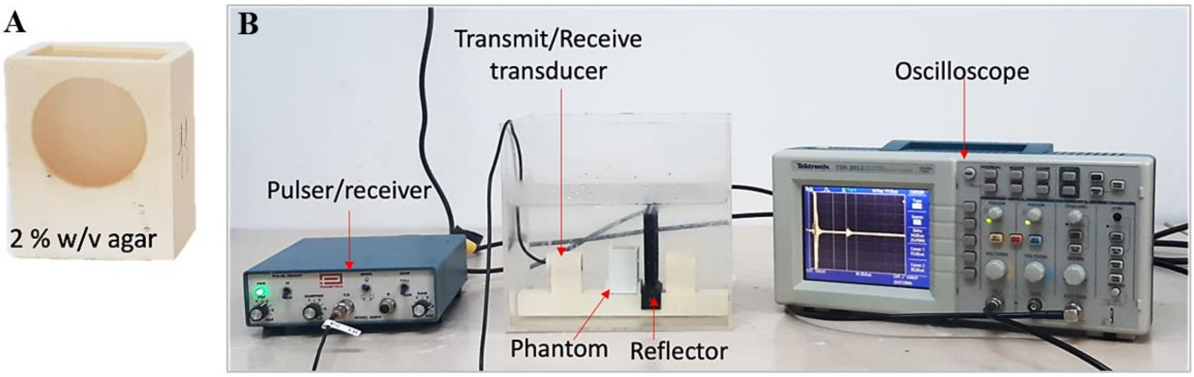

***Figure 2**: (A) Indicative photo of the 2% w/v agar phantom in the dedicated mold. (B) Experimental set-up used for measuring ultrasonic propagation speed.*

The echoes were recorded in the reference water path and with each phantom fixed on the holder. The group velocity of each phantom was calculated using Equation 1:

$$v_s = v_w \left[\frac{(t_w - t_s)}{\Delta t} + 1 \right] \quad (1)$$

where v_w is the ultrasonic propagation speed in water, t_w is the time needed for the wave to travel to the reflector and back to the transducer in the reference water path, t_s is the time needed for the wave to travel the same distance in the presence of the phantom, and Δt is the time difference between the echoes arising from the front and back surfaces of the phantom. For both transducers, the propagation speed of ultrasound in water (v_w) was measured by analysing echo signals recorded in the reference water path. For each phantom, five measurements (n=5) of the ultrasonic propagation speed were obtained.

Ultrasonic attenuation

The attenuation coefficient of each phantom was measured using a through-transmission method at two different frequencies: 1.1 and 2.2 MHz. For measurements at 1.1 MHz, the 2.7 MHz planar transmitter transducer (Piezo Technologies) and a 1.1 MHz planar receiver transducer (diameter of 30 mm, in-house, element from CeramTec, Plochingen, Germany) were connected to the function generator (TG550, Thurlby Thandar Instruments, Huntingdon, UK) and oscilloscope (TDS 2012, Tektronix, Inc.), respectively. Attenuation measurements at 2.2 MHz were executed using a pair of identical 2.2 MHz planar transducers (diameter 10 mm, in-house, element from QX Ultrasonic, Beijing, China). **Figure 3** illustrates the experimental set up utilized for measuring the attenuation coefficient.

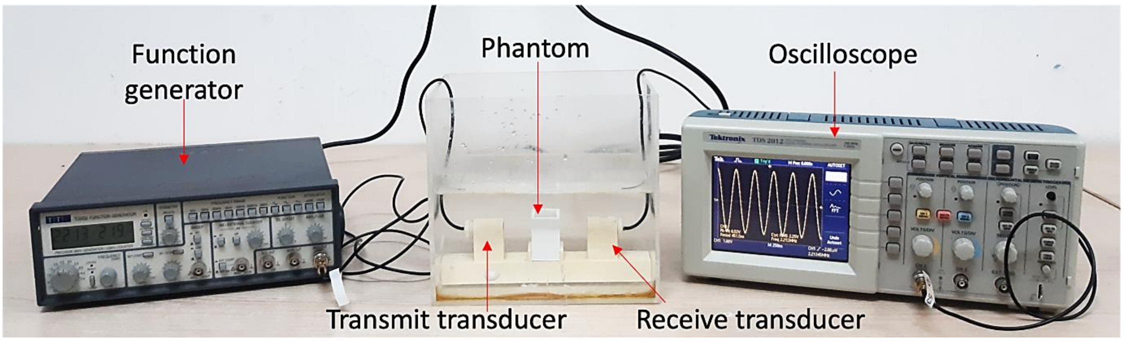

***Figure 3**: Experimental set-up used for measuring the attenuation coefficient.*

The acoustic impedance of each phantom (Z) was initially calculated by multiplying the measured mass density (ρ) with the ultrasonic propagation speed (v_s). Thereafter, the reflection coefficient of each phantom (R) was calculated using Equation 2:

$$R = (\frac{Z_1 - Z_2}{Z_1 + Z_2})^2 \tag{2}$$

where Z_1 is the acoustic impedance of water calculated by multiplying the density of water with the ultrasonic propagation speed in water and Z_2 is the calculated acoustic impedance of the investigated phantom. Accordingly, the transmission coefficient (T) was calculated using Equation 3:

$$T = 1 - R \tag{3}$$

With the transmission-through method, signals at each frequency were initially recorded in the reference water path and then with each phantom placed between the two transducers. The attenuation coefficient (a_s) was calculated using Equation 4:

$$a_s = a_w + \frac{20\, loge}{x} * ln\left(\frac{A_w}{A_s}T\right) \tag{4}$$

where a_w is the attenuation coefficient of water, x is the thickness of the phantom (2.6 cm), A_w is the signal received in the reference path, A_s is the signal received in the presence of the phantom and T is the transmission coefficient. For each phantom, five (5) individual signal measurements were recorded.

1.2.3 Thermal Properties

The main thermal properties (i.e., thermal conductivity, specific heat capacity, and thermal diffusivity) of each phantom were automatically measured using a portable heat transfer analyser (ISOMET 2114, Applied Precision, Bratislava, Slovakia) with a dedicated needle probe (IPN 1100, range 0.2-1 W/m.K, Applied Precision). The needle probe was inserted in its entirety, centrally along the longitudinal axis of each phantom (dimensions of 6 cm in width, 15 cm in length, and 6 cm in height). For each phantom, six (6) individual measurements were acquired. **Figure 4** shows a photo of the relevant experimental setup.

***Figure 4**: The experimental set-up used to measure the thermal properties of each agar-based phantom.*

1.2.4 MRI relaxation properties

In this experimental part, the various agar/silica gels were developed in the dedicated multicompartment container shown in **Figure 5A**. Water, oil and air served as reference materials. For relaxation time mapping, a series of T1-Weighted (T1-W) Inversion Recovery (IR) and T2-Weighted (T2-W) Spin Echo (SE) images of the phantoms were acquired in a 3T

Siemens scanner (Magnetom Vida, Siemens Healthineers, Erlangen, Germany) utilizing the Head-Neck imaging coil (HeadNeack_64_CS, Siemens Healthineers). The phantom container was positioned inside the coil cavity, as illustrated in **Figure 5B**.

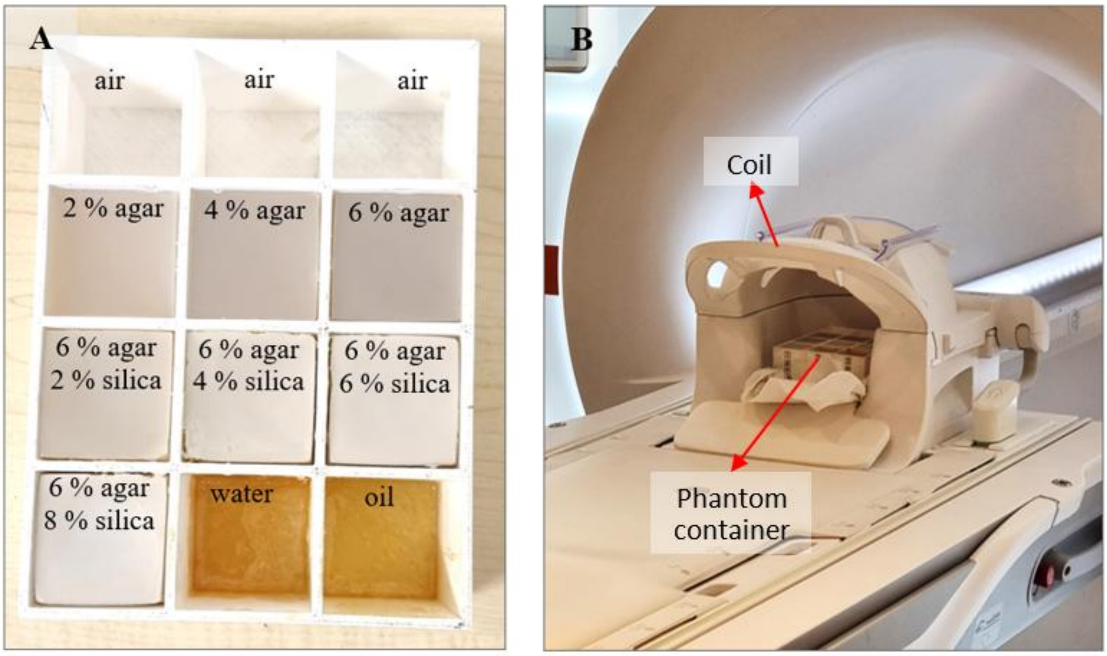

Figure 5*: (A) Photo of the phantoms and their compositions. (B) Experimental set-up inside the 3 T MRI scanner for relaxation time mapping.*

A 2D multiecho T2-W SE imaging sequence was employed for mapping the transverse relaxation time. Multiple coronal scans were obtained at variable Echo Time (TE) values to demonstrate the transverse magnetization exponential decay. The images were acquired with the following parameters: Repetition time (TR) = 2500 ms, TE = 8.5-255 ms (8.5 ms step), flip angle (FA) = 180°, echo train length (ETL) = 30, pixel bandwidth (pBW) = 300 Hz/pixel, matrix size = 256×218, field of view (FOV) = 180×180 mm^3, slice thickness = 5 mm, and number of excitations (NEX) = 1. Signal intensity (SI) measurements were performed for individual voxels on each acquired image. Automated algorithms were employed to fit the SI measurements to the equation that describes how the transverse magnetization (M_{xy}) reduces to 37 % of its reference value (M_0) [18]. T2 relaxation times were then measured from the generated parametric maps by fitting ROIs on each phantom and measuring average values.

A region of interest (ROI) approach was followed for measuring T1 relaxation times. T1W IR SE images of the phantoms were obtained at variable Inversion Time (TI) values: 50, 200, 500, 600, 650, 700, 725, 750, 775, 800, 825, 850, 900, 1000, 1100, 1200, 1500, 1900, and 2400 ms, while the rest parameters were set as follows: TR = 2500 ms, TE = 20 ms, FA = 70°, ETL = 1, pBW = 250 Hz/pixel, matrix size = 256×72, FOV = 220×206 mm^2, slice thickness = 10 mm, and NEX = 1. Acquired images were processed with a DICOM viewer software (MicroDicom, MicroDicom Ltd, Sofia, Bulgaria) and circular identical ROIs were consistently drawn on each phantom. The average SI in the ROI was measured in each case and inserted into an Excel spreadsheet. A graph of measured SI against TI was plotted for each phantom. For each TI, the modelled SI was calculated using the equation describing how the longitudinal magnetization (M_z) recovers to 63 % of its reference value (M_{0z}) [18]. For each phantom, the modelled SI plot was fitted on the plotted measured SI values and the T1 relaxation time was determined by adjusting the reference T1 value using the Solver add-in.

1.3 Evaluation of heating in phantoms of different agar/silica concentrations

1.3.1 MR thermometry

In this experiment, we investigated the influence of agar and silica concentrations on the focal temperatures generated by high-power sonication within agar-based phantoms inside the 3T Siemens MRI scanner (Magnetom Vida). Temperature measurements were obtained using MR thermometry. A water tank with specially designed containers for the phantoms and a holder for the transducer was placed on the MRI table. A 1 MHz single element spherically focused ultrasonic transducer (diameter = 50 mm, radius of curvature = 80 mm, and efficiency = 32.5 %.) was fitted at the bottom part facing towards the bottom of the phantoms and was connected to an RF amplifier (AG1016, AG Series Amplifier, T & C Power Conversion, Inc., Rochester, USA) situated outside of the MRI room. The receiver coil (Ultraflex 18-channel small coil, Siemens Healthineers) was securely positioned a few cm above the water container. **Figure 6A** shows the aforementioned containers filled with gel phantoms of varying agar concentration (top view), and **Figure 6B** shows the relevant experiment setup.

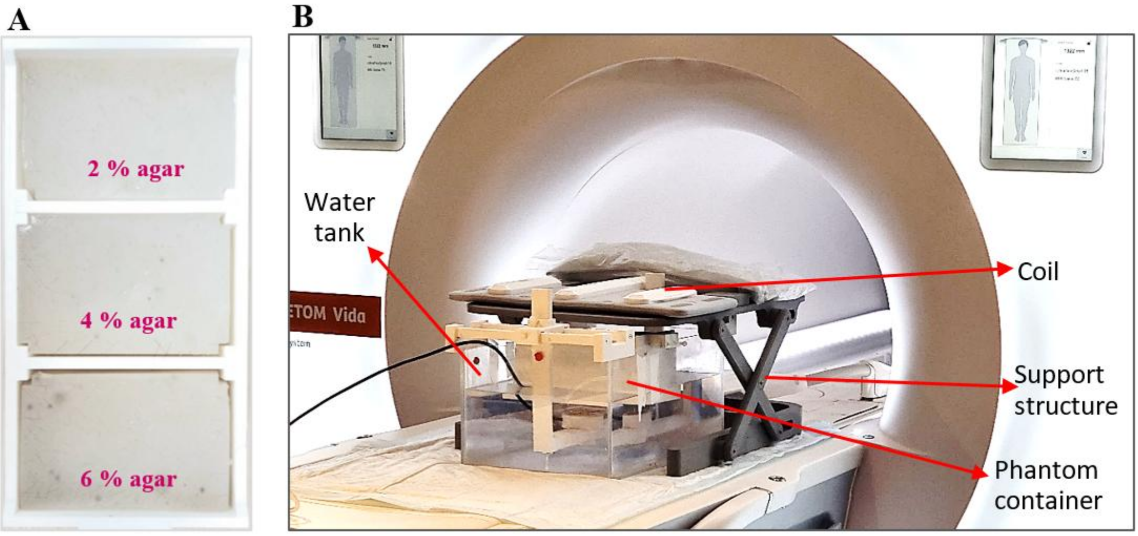

Figure 6*: (A) Top photo of the holder containing the 3 different agar phantoms. (B) Experimental set-up for phantom sonication arranged inside the 3 T MRI scanner.*

Each agar/silica phantom was exposed to a single sonication at 200/ 300 W electric power (acoustic power of 65/ 97.5 W) for 30 s at a focal depth (FD) of 40 mm. 2D Fast Low Angle Shot (FLASH) images were acquired for MR thermometry monitoring during the heating period (30/60 s) and a subsequence cooling period (30/60 s), with the following parameters: TR = 25 ms, TE = 10 ms, FA = 30°, ETL = 1, pBW = 250 Hz/Pixel, matrix size = 96 x 96, FOV = 280×280 mm^2, slice thickness = 3 mm, NEX = 1, and acquisition time = 2.4 s.

1.3.2 Lesion visualization by high resolution imaging

Post-sonication T2-W Turbo Spin Echo (TSE) images were acquired in coronal and axial planes for lesion assessment. The employed sequence parameters were TR = 4000-7000 ms, TE = 52 ms, FA = 110°, ETL = 30, pBW = 250 Hz/Pixel, matrix size = 256 x 256, FOV = 260 x 260 mm^2, slice thickness = 3 mm, and NEX = 2.

The regression of phantom lesions on MRI images with time was evaluated as well. It should be noted that for the specific experimental part, sonications were performed utilizing a 2.6 MHz transducer (diameter = 50 mm, radius of curvature = 65 mm, and efficiency = 30%).

1.4 Tumor bearing brain/skull phantom

After conducting preliminary experiments to evaluate the key properties (acoustic, thermal, MRI) and heating capacity of phantoms with varying inclusion concentrations, we proceeded to develop the tumor-bearing head phantom. This phantom comprises a skull mimic filled with agar-based tissue-mimicking material, with an embedded tumor mimic. The selection of agar/silica concentrations for the brain tissue and tumor-mimicking materials was based on the outcomes of our preliminary assessment (described in previous sections).

1.4.1 Development Process and Material Composition Selection

A two-compartment skull phantom was produced through rapid prototyping. The skull bone model was derived by segmenting computed tomography (CT) head scan images from an anonymized female volunteer. A circular segment of the temporal-parietal skull area was isolated (referred to as circular skull insert), resulting in a two-compartment skull model. The designed skull model was 3D-printed with 100% infill and filled with a tissue mimicking material to form the head phantom. Indicative photos of the 3D printed skull with and without the circular skull insert can be seen in **Figure 7A**. Notably, the circular skull insert can be easily removed to expose the brain-tissue phantom, allowing sonication through the skull mimic or in free field. A spherical gel-based tumor mimic, with a diameter of 20 mm, was created by molding in a dedicated mold featuring the relevant cavity, as depicted in **Figure 7B**. This mimic was embedded in the phantom during the manufacturing process to simulate a brain tumor.

The stereolithography format of the circular skull insert underwent processing to uniformly adjust its thickness to 1 mm across its entire surface (diameter of 60 mm). The 1-mm thick skull mimic was then 3D printed with the following thermoplastic materials: Resin (Photon M3 Max SLA printer, Anycubic, China), PLA (Raise3D E2 FDM printer, Raise3D, CA, USA), ASA (F270 FDM industrial printer, Stratasys, Minnesota, USA), CPE+ (3 Extended Ultimaker FDM printer, Utrecht, Netherlands), and TPU (3 Extended Ultimaker). **Figure 7C** is a photo of the various 1-mm skull mimics.

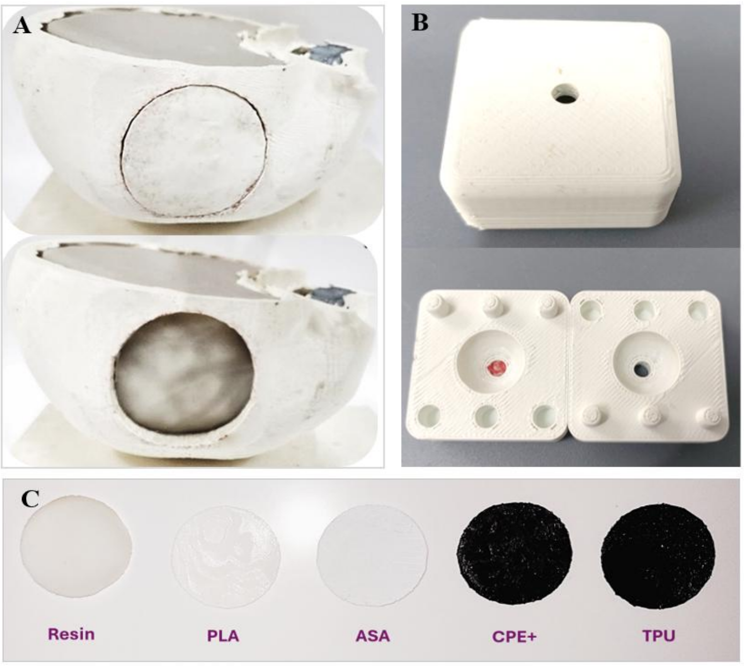

Figure 7*: (A) Photos of the developed skull phantom filled with gel-based material with the skull insert attached to the relevant cavity (top) and without it (bottom). (B) Photos of the tumor mold; exterior and interior view, utilized for manufacturing the spherical tumor mimic. (C) Photo of the 3D printed thermoplastic circle-shaped skull inserts.*

After thoughtful review of the initial findings from assessing the diverse agar/silica phantoms, the recipe consisting of 6% w/v agar and 4% w/v silica was selected to mimic the tumor. For mimicking normal brain tissue in the surrounding, a pure agar gel of 6% w/v was chosen. The concentration of these inclusions was shown to impart the desired phantom characteristics for the specific application of brain MRgFUS.

The selection of inclusion composition was determined by multiple criteria. Firstly, the attenuation coefficient of the brain tissue mimicking material (6% agar) at 1 MHz; a frequence commonly used in transcranial applications, was measured to be 0.743 ± 0.027 dB/cm (section 2.2.1), aligning sufficiently with reported literature values for brain tissue, which typically range around 0.8 dB/cm [19]. Secondly, both selected recipes yielded sufficiently high temperature increases (to ablative levels) using typical ultrasonic parameters (i.e., 200 W el. power for 30 s). More importantly, there was a significantly higher heat accumulation and resultant temperature increase observed in the silica-doped (4%) phantom compared to the pure 6% agar gel. In addition, the specific inclusion compositions provided excellent contrast between the tumor mimic and its surroundings in high-resolution MRI scans. It is also notable that higher silica concentrations (6% and 8%) did not result in a further increase in temperature. Additionally, these concentrations led to increased stiffness, potentially rendering them too stiff compared to soft tissue. As a result, these recipes were not selected for mimicking tumors.

1.4.2 Preliminary MRI evaluation

These experiments aimed to evaluate: 1) the MRI features of the developed tumor-bearing phantom, and 2) the focal temperatures generated by high-power sonications within the tumor mimic, both through the skull insert and in free field, using MR thermometry, in order to demonstrate the phantom's suitability for its intended application.

A 3D printed water tank with integrated compartments was designed to securely hold the ultrasonic transducer (frequency = 1 MHz, diameter = 50 mm, radius of curvature = 80 mm, and efficiency = 32.5 %) beneath the developed tumor-bearing brain/skull phantom to facilitate measurements. The transducer was driven by an RF amplifier (AG1016, AG Series Amplifier) situated outside of the MRI room. **Figure 8** shows the water tank and compartments. Note that in this figure, the skull mimic appears empty; before filling it with the gel.

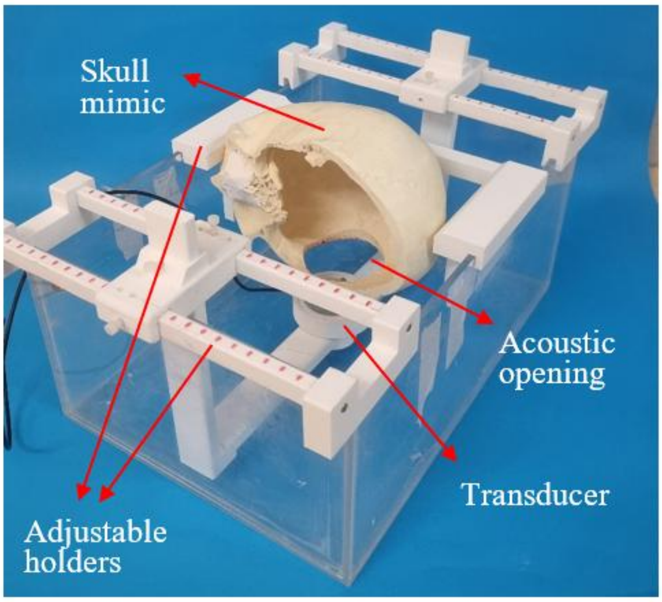

Figure 8: *Photo of the water tank with integrated compartments used for phantom sonications.*

The relevant experimental setup for tumor sonications under MR thermometry is shown in **Figure 9**. The water tank was placed on the table of the scanner (3 T Magnetom Vida) and filled with degassed water to achieve proper ultrasonic coupling between the transducer and bottom surface of the phantom. The imaging coil (Ultraflex 18-channel small coil) was securely placed at a small distance (few cm) above the skull mimic supported by a dedicated structure.

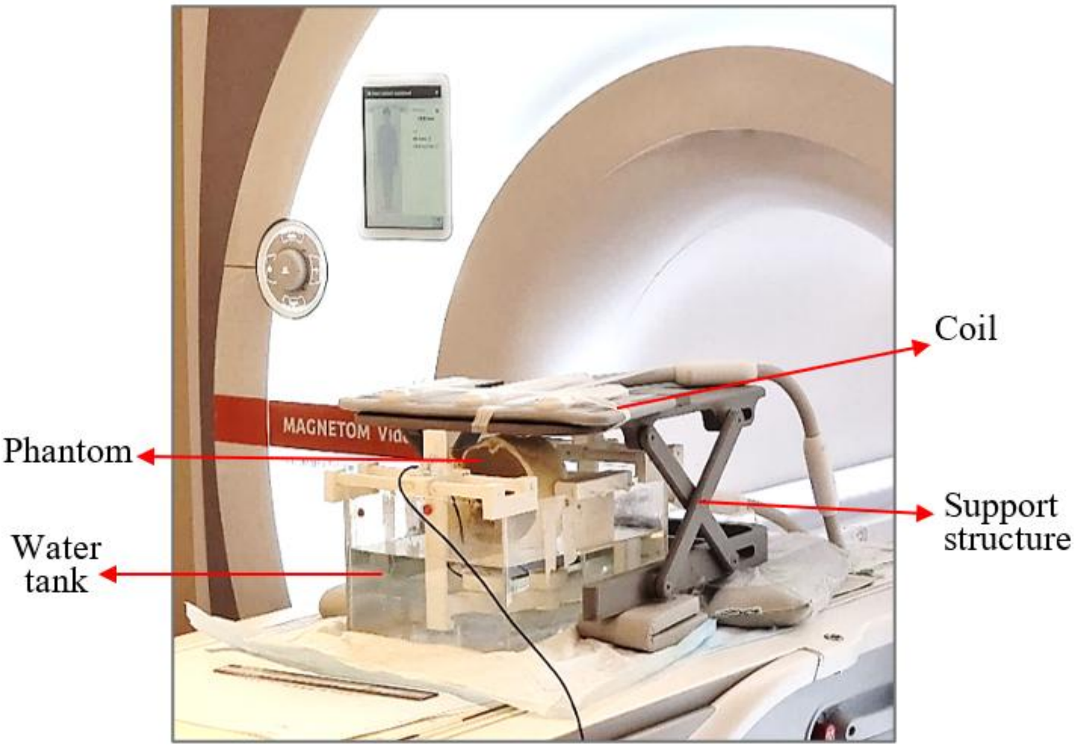

Figure 9: *Experimental setup inside the 3 T MRI scanner for sonications in the tumor-bearing brain tissue/skull phantom.*

Imaging features

A high resolution T2-W TSE sequence was employed to evaluate the overall MRI appearance of the phantom and tumor mimic contrast relative to the surrounding. Images were acquired with the following parameters: TE = 52 ms, FA = 110^o, NEX = 2, FOV = 260 x 260 mm^2, Slice thickness = 3 mm, Matrix = 256 x 256, ETL = 30, pBW = 250 Hz/Pixel, and TR = 3240 ms/ 2000 ms/ 8530 ms for coronal, axial and sagittal imaging, respectively.

Assessment of thermal heating

High power sonications were conducted in free field, as well as through the 3D-printed skull mimics made from different thermoplastic materials, with MR thermometry employed for precise temperature measurements. The thermometry results were compared between the skull mimics and the free field conditions (i.e., no skull mimic). The relevant coronal and axial FLASH images were acquired employing parameters similar to those reported in section 1.3. Electric power levels ranging from 200 to 300 W were applied for durations of 30 or 60 s.

2. RESULTS

2.1 Characterization of agar/silica phantoms

2.1.1 Acoustical properties

Ultrasonic propagation speed

Table 1 summarizes the experimental measurements of ultrasound propagation speed for the various agar/silica phantoms, taken at 2.2 and 2.7 MHz. The values are presented as means with the corresponding standard deviation. The measured density of each phantom is also listed in the table. The ultrasonic propagation speed was found to exhibit an almost linear increase with agar concentration at both frequencies, as illustrated in **Figure 10A**. Additionally, **Figure 10B** depicts a slight speed enhancement with rising silica concentration.

Table 1*: Measured Mass density and Ultrasonic propagation speed for each different phantom.*

	Frequency (MHz)	***2.2***	***2.7***
Recipe	**Density (kg/m^3)**	**V_s (m/s)**	**V_s (m/s)**
2 % agar	901.7	1513.0 ± 0.1	1514.1 ± 0.1
4 % agar	1030	1520.7 ± 0.3	1519.8 ± 0.6
6 % agar	1172	1531.0 ± 0.5	1531.4 ± 0.2
6 % agar, 2 % silica	981.4	1530.0 ± 0.6	1531.2 ± 0.4
6 % agar, 4 % silica	1021.7	1530.2 ± 0.2	1532.3 ± 0.2
6 % agar, 6 % silica	1160	1530.9 ± 0.1	1532.6 ± 0.2
6 % agar, 8 % silica	1183.3	1531.2 ± 0.3	1532.7 ± 0.2

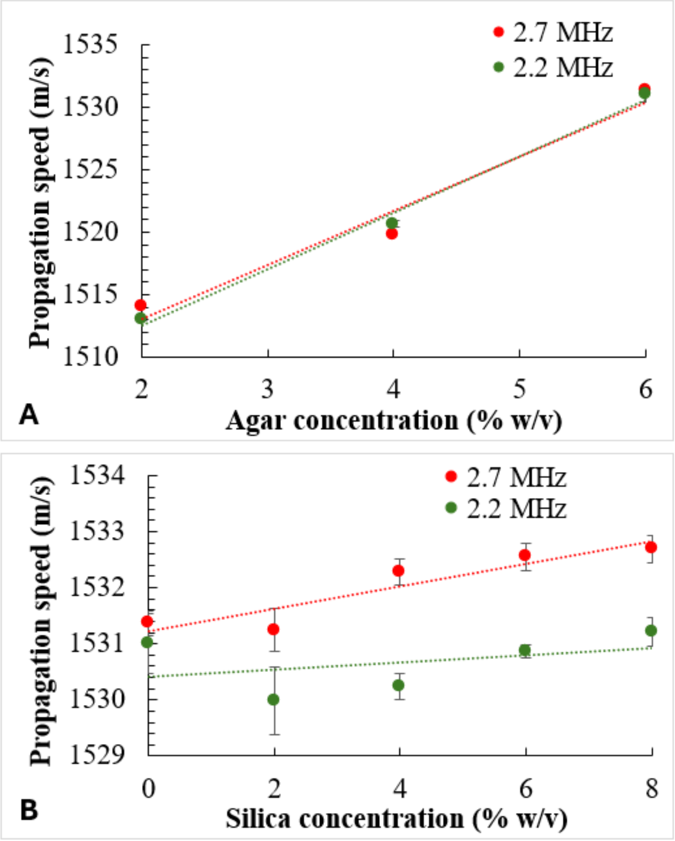

Figure 10*: Mean ultrasonic propagation speed of (A) agar-based phantoms developed with varied agar concentration (2, 4, or 6 % w/v) and (B) 6 % w/v agar phantoms doped with varying silica concentration (2, 4, 6 or 8 % w/v) at 2.2 and 2.7 MHz.*

Ultrasonic attenuation

The estimated acoustic impedance and ultrasonic attenuation values estimated for the various agar/silica phantoms at 1.1 and 2.2 MHz are listed in **Table 2.** The ultrasonic attenuation values are presented as means with the corresponding standard deviations.

***Table 2**: Estimated acoustic impedance and ultrasonic attenuation of each phantom at 1.1/ 2.2 MHz.*

Frequency (MHz)	***1.1***	***2.2***	***1.1***	***2.2***
Phantom	**Acoustic impedance (MRayls)**		**Mean attenuation (dB/cm)**	
2 % agar	1.36	1.36	0.20 ± 0.06	0.63 ± 0.02
4 % agar	1.57	1.57	0.45 ± 0.04	0.90 ± 0.07
6 % agar	1.80	1.79	0.74 ± 0.03	1.42 ± 0.04
6 % agar, 2 % silica	1.50	1.50	1.03 ± 0.06	1.71 ± 0.05
6 % agar, 4 % silica	1.57	1.56	1.21 ± 0.03	1.97 ± 0.05
6 % agar, 6 % silica	1.78	1.78	1.31 ± 0.02	2.15 ± 0.05
6 % agar, 8 % silica	1.81	1.81	1.48 ± 0.02	2.73 ± 0.07

The findings indicate that at both frequencies, the attenuation increases with higher agar and silica concentrations, following an almost linear trend, as illustrated in **Figures 11A** and **Figure 11B**, respectively. As expected, a significantly higher level of ultrasonic attenuation was observed at the higher frequency (2.2 MHz).

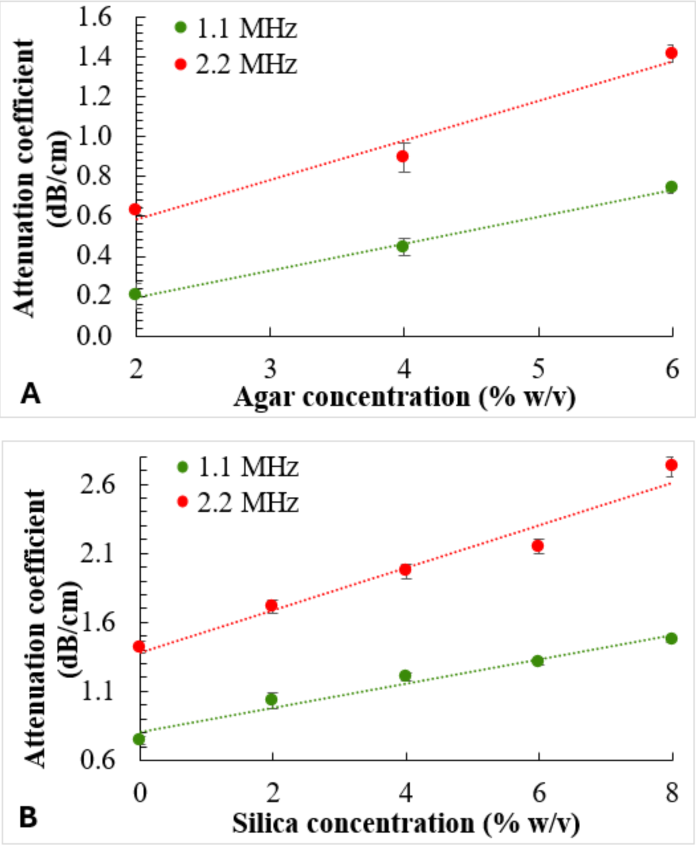

***Figure 11**: Mean ultrasonic attenuation coefficient of (A) agar-based phantoms developed with varying agar concentration (2, 4, or 6 % w/v) and (B) 6 % w/v agar phantoms doped with varying silica concentration (2, 4, 6 or 8 % w/v), as measured at 1.1 and 2.2 MHz. Values are expressed as means with errors bars representing the corresponding standard deviations.*

2.1.2 Thermal Properties

The mean values (n=6) of measured thermal properties of the various phantoms are summarized in **Table 3**. **Figure 12A** illustrates the thermal conductivity plotted against silica concentration, demonstrating a clear linear increase (R^2=0.99). A comparable observation was noted for the thermal diffusivity plot in **Figure 12B** (R^2=0.98).

Table 3*: Measured thermal properties of each agar/silica phantom.*

Recipe	Thermal conductivity (W/mK)	Specific heat capacity (10^6 J/m^{3}K)	Thermal diffusivity (10^{-6} m^2/s)
2 % agar	0.545 ± 0.016	1.876 ± 0.007	0.291 ± 0.008
4 % agar	0.530 ± 0.007	1.875 ± 0.006	0.283 ± 0.004
6 % agar	0.524 ± 0.002	1.872 ± 0.008	0.280 ± 0.001
6 % agar, 2 % silica	0.539 ± 0.001	1.881 ± 0.006	0.286 ± 0.001
6 % agar, 4 % silica	0.550 ± 0.001	1.893 ± 0.012	0.291 ± 0.002
6 % agar, 6 % silica	0.559 ± 0.002	1.906 ± 0.009	0.293 ± 0.002
6 % agar, 8 % silica	0.574 ± 0.001	1.910 ± 0.005	0.301 ± 0.001

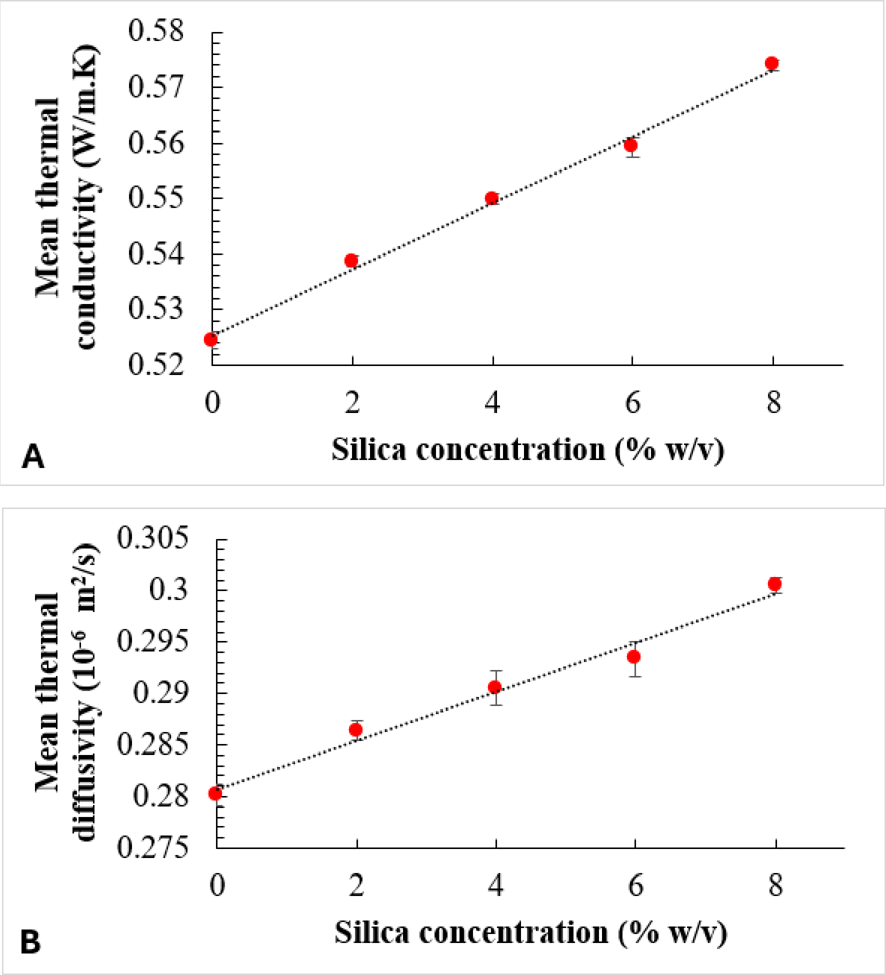

Figure 12*: (A) Thermal conductivity and (B) thermal diffusivity of 6 % w/v agar phantoms doped with varying silica concentration (2, 4, 6 or 8 % w/v). Values are expressed as means with errors bars representing the corresponding standard deviations.*

2.1.3 MRI relaxation properties

Figure 13 shows indicative T1-W IR SE coronal images acquired at various TIs within the examined range. Indicative graphs of the measured and modelled SI as calculated from the series of IR SE images plotted against TI (50-2400 ms) can be seen in **Figure 14**.

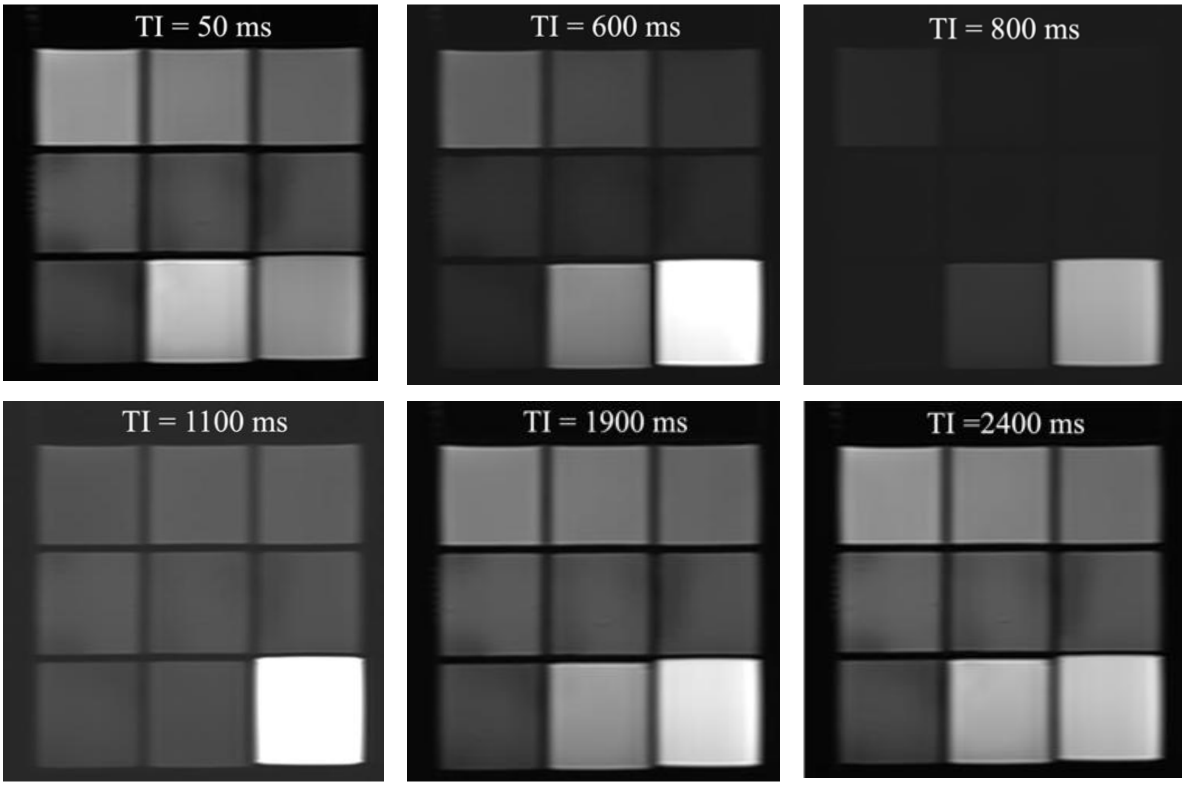

Figure 13*: Coronal T1-W IR SE images of the various agar/silica phantoms, water and oil acquired at varied TI values in the range of 50-2400 ms.*

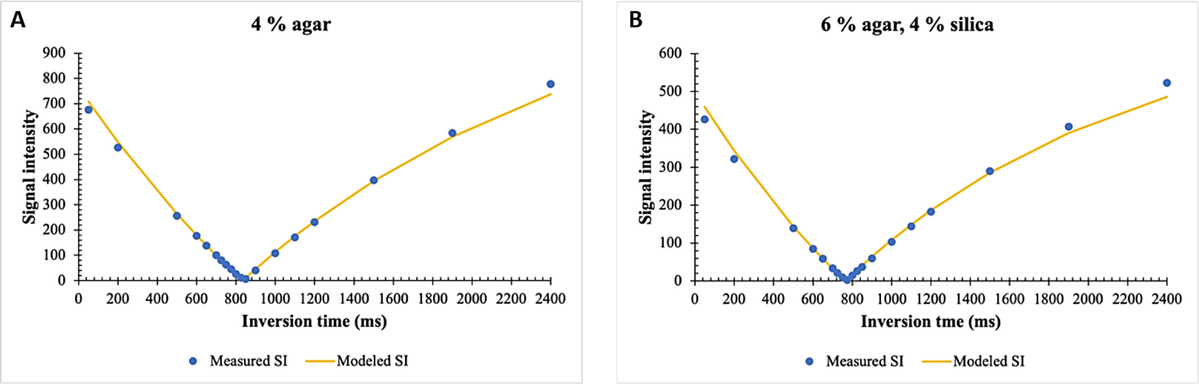

Figure 14*: Measured and modelled SI as calculated from T1-W IR SE images versus TI (50-2400 ms) for the phantoms containing (A) 4% agar and (B) 6% agar and 4% silica.*

Regarding T2 relaxation time mapping, the relevant parametric map, as generated by the voxel-by-voxel analysis of a series of T2-W SE images acquired at varied TE values (8.5-255 ms), is presented in **Figure 15**.

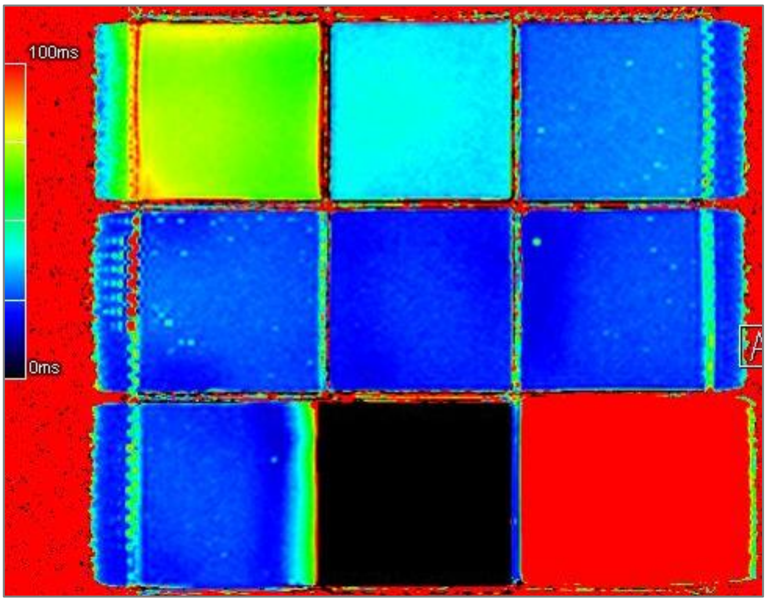

Figure 15*: T2 parametric map of different agar-based phantoms, water, and oil generated by voxel-based analysis of a series of T2-W SE images acquired at varied TE values (8.5-255 ms).*

Table 4 summarizes the estimated T1 and T2 relaxation times of the different phantoms, water, and oil. Note that, in contrast to silica, the chosen agar concentration significantly influenced the resulting MRI properties.

Table 4: *Estimated T1 and T2 relaxation times of each agar/silica phantom.*

Material	T1 (ms)	T2 (ms)
2 % w/v agar	2152.3	69.6
4 % w/v agar	1737.4	40.2
6 % w/v agar	1470.0	29.9
6 % agar, 2 % silica	1466.0	27.2
6 % agar, 4 % silica	1440.1	23.1
6 % agar, 6 % silica	1424.0	24.8
6 % agar, 8 % silica	1445.6	24.7
Water	2700.1	0
Oil	303.4	154.6

2.2 Evaluation of heating in phantoms of different agar/silica concentrations

2.2.1 MR thermometry

Figure 16 illustrates indicative MR thermometry results of sonication at 200 W for 30 s (acoustic power = 65 W, FD = 40 mm) in the phantom containing 6% w/v agar and 4% w/v silica, acquired in the coronal plane.

The recorded thermal profile at the focus during the heating and cooling periods is shown in Figure 16A. The temperature and thermal dose maps shown in Figure 16B and Figure 16C, respectively, were acquired after the completion of sonication, revealing the spatial distribution of temperature and accumulated thermal dose around the focal spot. The necrotic area, simulated based on thermal dose accumulation, is depicted in Figure 16D.

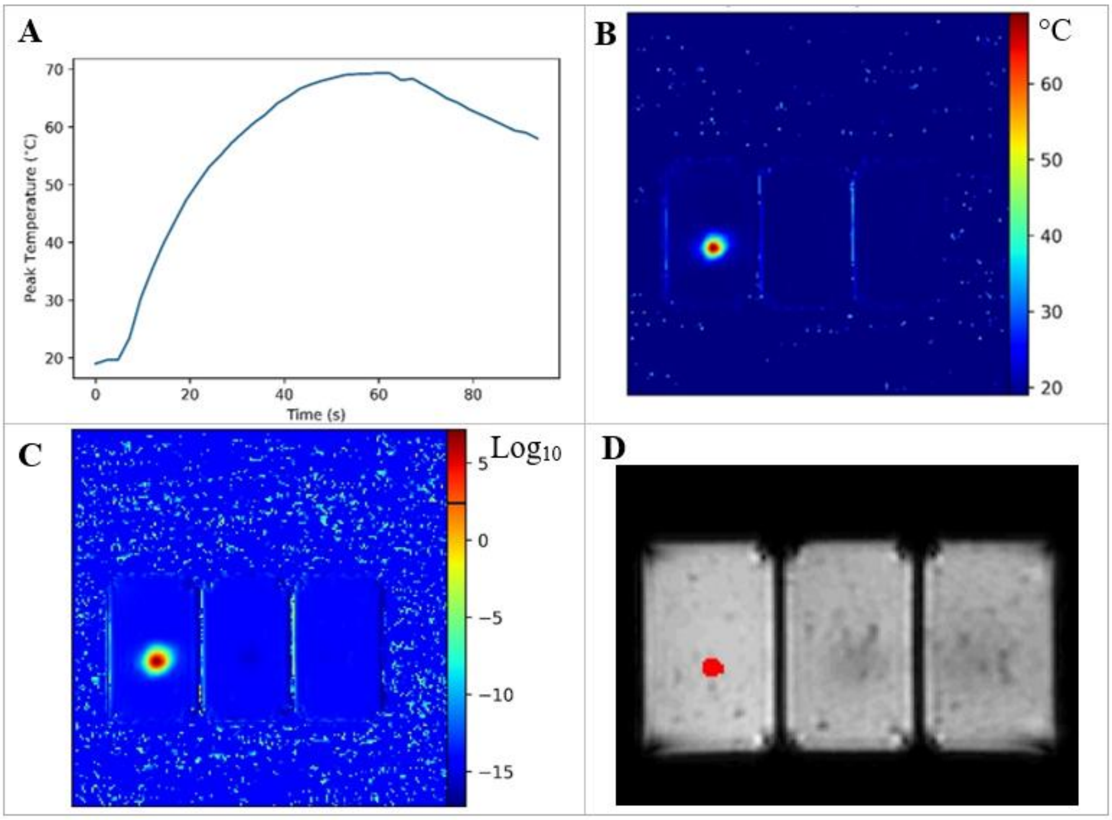

Figure 16: *(A) Focal temperature change within 4 % silica doped phantom during and after sonication (200 W, 30 s) with the 1 MHz transducer. (B) Colour-coded thermal map produced upon completion of sonication. (C) Colour-coded thermal dose map produced upon completion of sonication. (D) Simulated necrotic area upon completion of sonication (58.5 mm^2).*

The graph of **Figure 17** displays the focal temperature change achieved within agar phantoms by sonication at 200 W for 30 s plotted against the w/v agar concentration, compared with the corresponding change observed in a porcine tissue sample. Note that a three-fold increase in agar concentration (from 2 to 6 % w/v) leads to a slightly more than four-fold increase in temperature change.

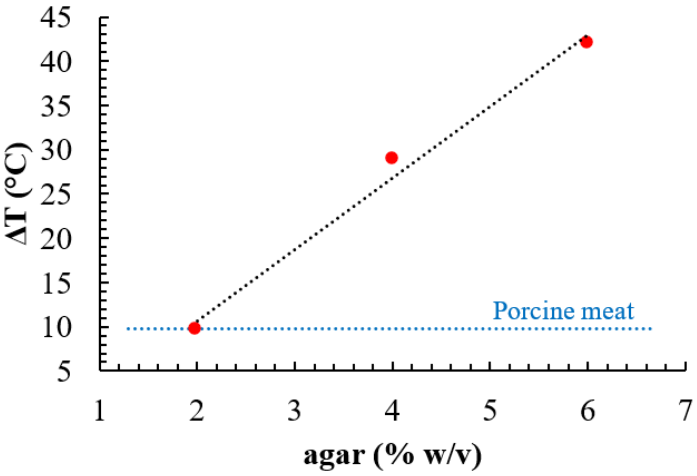

Figure 17: *Focal temperature change within agar phantoms of different w/v agar concentration following sonication at 200 W for 30 s. The blue dotted line represents the temperature change recorded in the pork tissue sample utilizing similar sonication parameters.*

Accordingly, **Figure 18** graphically illustrates how temperature changes are affected by increasing silica concentration. Contrary to agar, increasing the silica concentration within the range of 2% to 6% w/v results in a slight decrease in temperature change. It's worth noting that the phantom doped with 8% w/v silica does not follow this trend. **Table 5** summarizes the recorded temperature changes in the phantoms of different agar and silica concentrations.

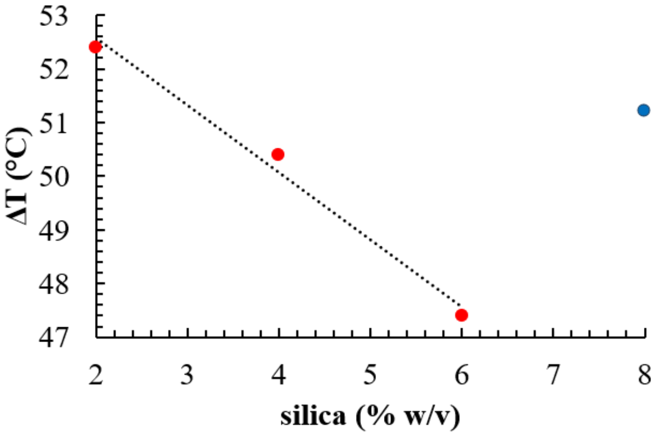

***Figure 18**: Focal temperature change within 6% w/v agar phantoms containing different w/v silica concentration following sonication at 200 W for 30 s.*

***Table 5:** Temperature change ΔT (°C) recorded in the various agar/silica phantoms (200 W, 30 s).*

Recipe	ΔT (°C)
2 % agar	9.6
4 % agar	28.8
6 % agar	42.0
6 % agar, 2 % silica	52.4
6 % agar, 4 % silica	50.4
6 % agar, 6 % silica	47.4
6 % agar, 8 % silica	51.2
Porcine meat	*9.8*

2.2.2 Lesion visualization by high resolution imaging

After sonication, we assessed the visibility and quality of lesion visualization on post-sonication T2-W images. Representative results are presented in **Figure 19.** Figure 19A illustrates T2-W coronal images of the three phantoms containing different silica concentrations immediately after sonication at 300 W for 60 s (acoustic power = 97.5 W, FD = 40 mm), as well as 20 minutes later. An indicative axial image acquired post sonication is shown in Figure 19B. These results are consistent with the thermometry data indicating that higher temperatures were generated in phantoms with higher silica concentrations. The comparison of images showcases the impact of silica concentration on contrast. This trend is graphically depicted in Figure 19C, where the normalized contrast-to-noise ratio (CNR) is plotted against the percentage of silica, revealing a second-order polynomial increase in CNR with increasing silica content (R^2=1). Additionally, it's observed that for higher silica content, the signal enhancement persists for a longer duration before returning to its original state (Figure 19A).

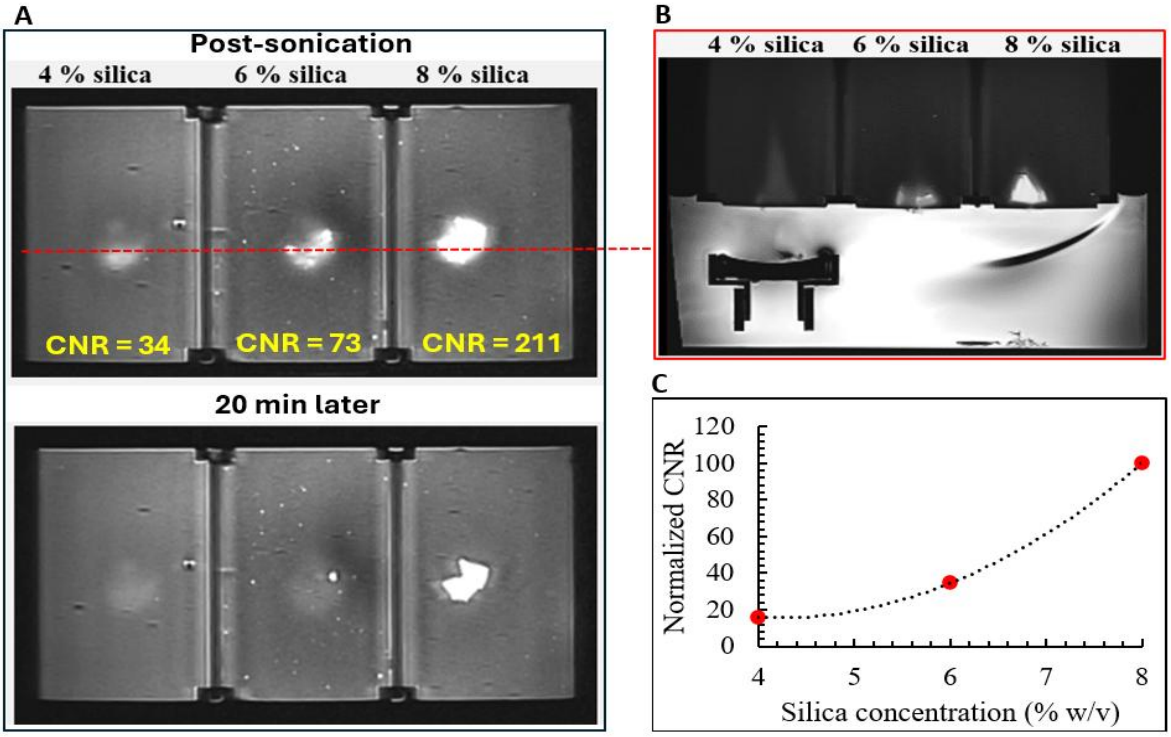

Figure 19*: (A) Coronal T2-W TSE images of the phantoms (6% w/v agar, varying silica) acquired after completion of sonications at 300 W for 60 s, and 20 min later (at 10-mm depth from sonicated surface with the 1 MHz transducer), revealing the inflicted lesions as areas of increased intensity at plane perpendicular to beam direction. (B) Axial T2-W TSE image, revealing the inflicted lesions at plane parallel to beam direction. The red dotted line indicates slice location. (C) Normalized CNR between lesion and surrounding versus silica concentration ($CNR = (SI_{lesion} - SI_{surrounding})/\sigma_{noise}$).*

After completion of sonication, lesions that appeared with increased intensity on T2-weighted images gradually faded until they disappeared. Lesion regression with time is illustrated in **Figure 20**, which shows a series of images acquired at different time points after sonication at 300 W for 60 s in the 6% w/v agar phantom, along with the graph of normalized SI versus time.

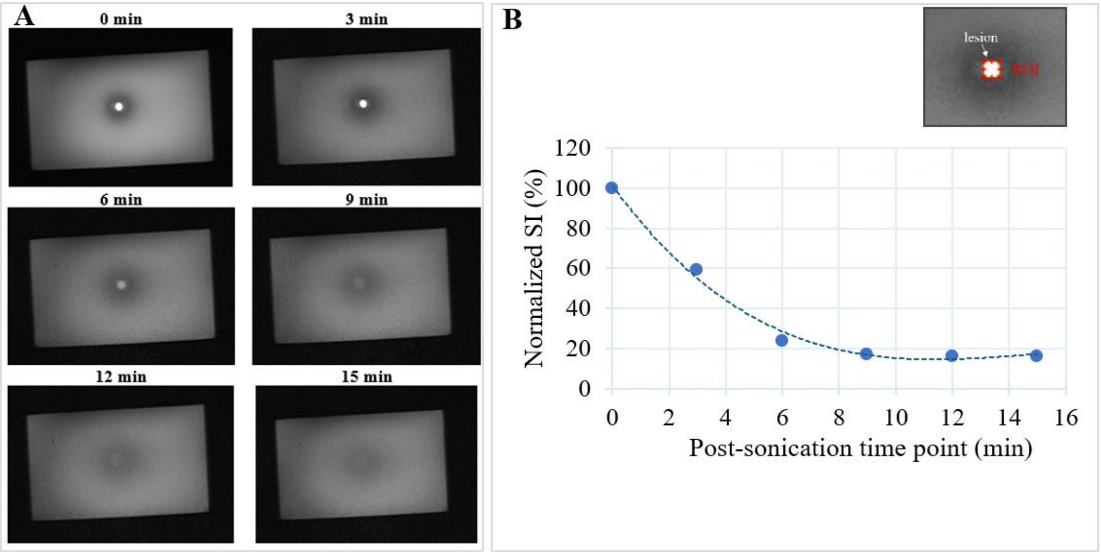

Figure 20*: (A) Series of coronal T2-W TSE images acquired over time following sonication (300 W, 60 s) with the 2.6 MHz transducer, revealing the regression of the lesion over time. (B) Plot of normalized SI of lesion versus post-sonication time as measured from the coronal T2-W images.*

2.3 Tumor bearing brain/skull phantom

2.3.1 Imaging features

Figure 21 presents MRI images of the developed tumor-bearing phantom in the 3 orthogonal MRI planes. Note that the tumor mimic appears as a well-defined area of decreased intensity, with excellent contrast from the surrounding tissue, owing to the inclusion of silica.

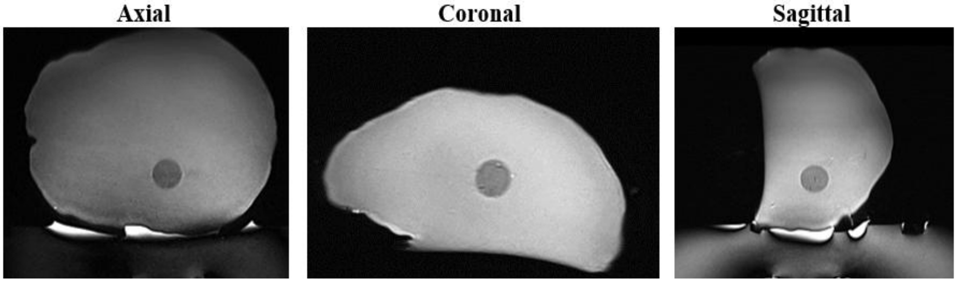

Figure 21: T2-W TSE images of the developed tumor-bearing brain/skull phantom in the three orthogonal MRI planes, with the spherical tumor mimic visualized as an area of decreased intensity.

2.3.2 Assessment of thermal heating

Indicative MR thermometry results from 1 MHz sonication within the tumor mimic (6% agar, 4% silica) at 250 W (acoustic power = 81 W, FD = 40 mm) for 30 s, as well as at a higher power of 300 W (acoustic power = 97 W) for 60 s are illustrated in **Figure 22**.

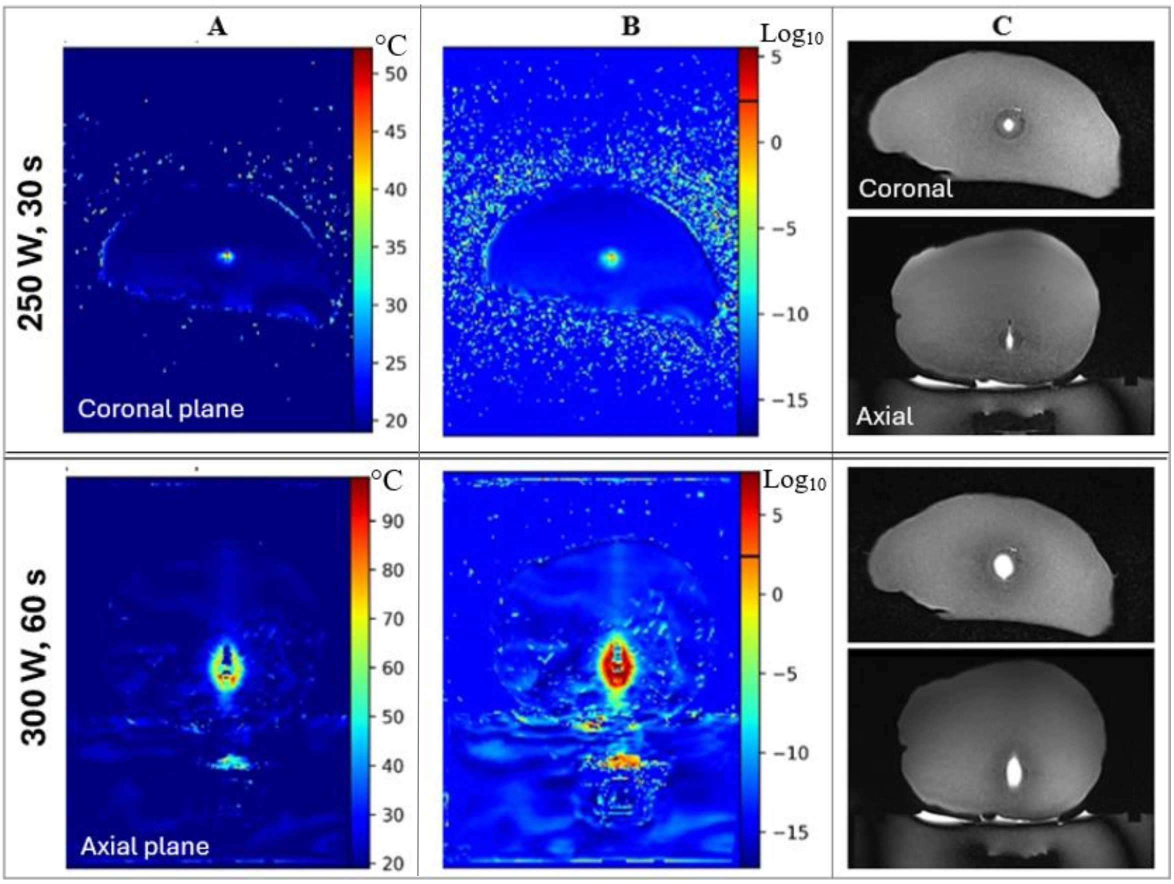

Figure 22: (A). Colour-coded thermal map produced upon completion of sonication in tumor mimic at 250 W (top) and 300 W (bottom). (B) Relevant colour-coded thermal dose maps . (C) Coronal and Axial T2-W TSE images of the phantom acquired after sonication at 250 W (top) and 300 W (bottom), revealing the inflicted lesions as regions of increased intensity.

The impact of incorporating the 1-mm skull mimics on focal temperature elevation and the distribution of accumulated thermal dose within and around the tumor can be observed in **Figure 23**, in comparison to the free field condition. In this indicative example, the tumor was exposed to 250 W for 30 s through the Resin and PLA inserts, and then without any skull mimic intervening in the beam path. It's noteworthy that the PLA skull attenuated the largest amount of ultrasonic energy. Consequently, in the phantom, the recorded temperature change decreased by more than threefold compared to the reference (from about 51°C to 15°C), with heat accumulating off-target and covering a large region outside the tumor. This indicates that the PLA skull induced significant beam defocusing effects. Conversely, the inclusion of the Resin skull in the beam path led to a mere 10-degree decrease in temperature change (ΔT ≅ 40°C) compared to free field sonication (ΔT ≅ 51°C), with heat predominantly accumulating in the tumor and minor off-target accumulation, thus showing promising potential for the proposed application.

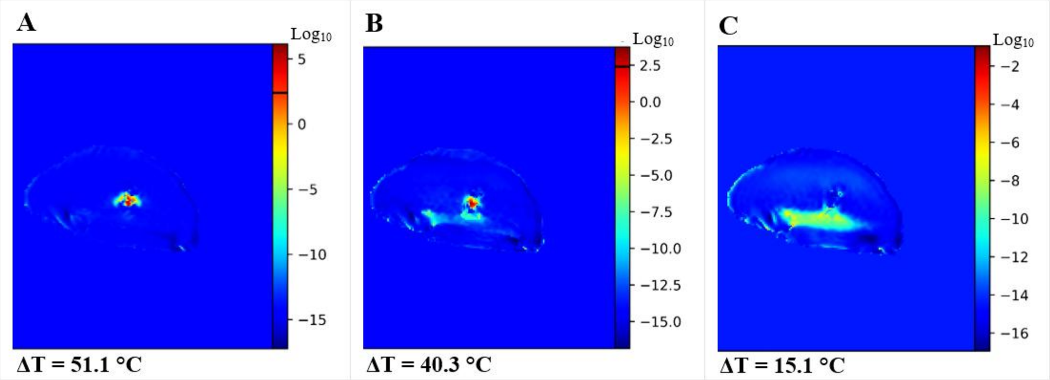

***Figure 23**: Colour-coded thermal dose map produced upon completion of sonication in tumor mimic at 250 W for 30 s (A) ın free field, (B) through the Resin skull, and (C) through the PLA skull. The corresponding temperature change is written at the bottom of each map.*

Finally, **Figure 24** compares T2-W TSE images of the phantom after sonication at 80 W acoustic power for 30 s without skull interference and with the 1-mm Resin skull mimic obstructing the beam. Notably, the thin Resin skull mimic allowed the creation of thin cigar shaped lesions within the tumor mimic.

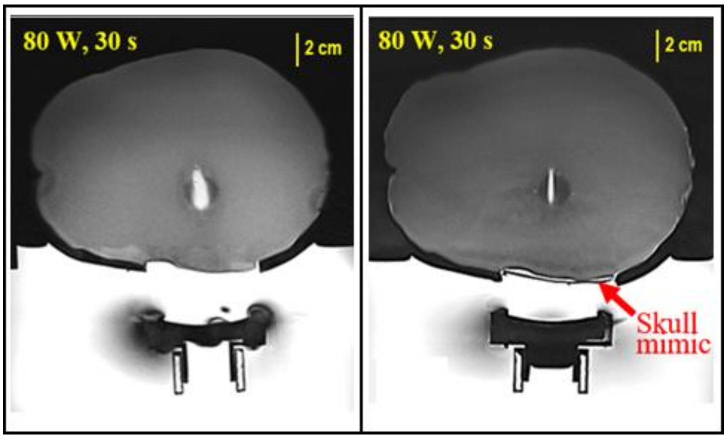

***Figure 24**: T2-W TSE images of the phantom after sonication of the tumor mimic at 80 W for 30 s without a skull mimic and through the resin skull.*

INTERPRETATION OF RESULTS

Seven (7) agar/silica phantoms have been developed and the impact of varying inclusion concentrations on their acoustic, thermal, and MRI relaxation properties has been investigated. The phantoms were prepared with either varying agar concentration (2%, 4%, and 6% w/v) or a constant amount of agar (6% w/v) and varying concentration of silica (2%, 4%, 6%, and 8% w/v). The ultrasonic propagation speed was found to exhibit an almost linear increase with agar concentration at both 2.2 and 2.7 MHz. Similarly, the findings suggest that attenuation increases proportionally with higher agar and silica concentrations at the examined frequencies of 1.1 and 2.2 MHz. Notably, the most significant impact of increasing agar concentration was evident in attenuation. Specifically, at 1.1 MHz, a three-fold increase in agar concentration (from 2 to 6% w/v) resulted in a slightly more than three-fold increase in the attenuation coefficient. Regarding thermal properties, it was observed that both thermal conductivity and thermal diffusivity increase linearly with increasing silica concentration. However, the effect is not particularly pronounced.

The candidate agar/silica phantoms were then examined regarding their response to thermal heating. Each phantom underwent a single high-power sonication using a single-element spherically focused transducer operating at 1 MHz, while being monitored with MR thermometry in a 3T MRI scanner. The recorded thermal profiles showed a realistic trend in terms of the rate of temperature increase and post-sonication decrease. Increasing agar concentration drastically increased the recorded temperature change, with a three-fold increase in agar concentration (from 2 to 6 % w/v) leading to a slightly more than four-fold increase in temperature change. Importantly, higher temperature changes were observed in all silica-doped phantoms (compared to pure agar gels); however, increasing the silica concentration within the range of 2% to 6% w/v resulted in a slight decrease in temperature change.

The visibility and quality of lesion visualization on post-sonication T2-W images was evaluated as well. Lesions appeared as well-defined regions of signal enhancement, with their dimensions determined by the applied ultrasonic parameters (i.e., power and sonication time), gradually fading over time until disappeared. The CNR between the lesion and surrounding tissue exhibited a second-order polynomial increase with increasing silica concentration. Additionally, at higher silica concentrations, the signal enhancement persisted for a longer duration before returning to its original state. Overall, the proposed phantoms were demonstrated to provide excellent lesion visualization on post-sonication T2-W TSE images.

After assessing the various agar/silica phantoms and analysing the acquired results, a tumor-bearing brain/skull phantom was developed. This involved the creation of a realistic skull mimic, fabricated via 3D printing. The mimic was designed as a two-compartment structure, featuring a removable circular insert. This insert was 3D printed using 5 different thermoplastic materials (Resin, PLA, ASA, CPE+, and TPU), each with a thickness of 1 mm. This design allowed for sonication through the different skull mimics as well as in free field conditions (i.e., without the skull). The rationale for exploring the use of a 1 mm skull insert lies in the potential to facilitate FUS ablation of unresectable brain tumors through the temporary removal of a small portion of the skull and its replacement with a thin, biocompatible skull insert.

The skull phantom was filled with an agar-based gel embedding a tumor simulator. The brain tissue mimicking material consisted of a pure 6% w/v agar gel, while for the tumor mimicking material, a mixture of 6% agar and 4% silica was deemed appropriate. The main reasons for selecting the specific inclusion composition are as follows: 1) Both recipes yielded sufficiently high temperature increases (ablative levels) using typical ultrasonic parameters (200 W el.

Power for 30 s). 2) There was a significantly higher heat accumulation and resultant temperature increase observed in the 4% silica-doped phantom compared to the pure agar gel. In other words, the selected recipes were deemed suitable in terms of achieving a different thermal response to heating between the tumor and normal tissue materials. 3) The inclusion compositions provided excellent contrast between the tumor mimic and its surroundings in high-resolution MR imaging. Furthermore, higher silica concentrations (6% and 8%) did not result in a further increase in temperature, while also leading to increased stiffness, potentially rendering them too stiff to accurately mimic soft tissue. Another factor considered was the estimated attenuation property of the 6% agar gel, measured at 0.743 ± 0.027 dB/cm (section 2.2.1), at 1 MHz—the frequency commonly utilized in transcranial applications. This measurement contributed to the decision to use the specific recipe for replicating brain tissue, as it closely aligns with reported values for brain tissue in the literature, typically around 0.8 dB/cm [19].

The incorporation of silica into the tumor mimic has proven effective in enhancing contrast in MRI imaging, resulting in excellent tumor visualization and facilitating precise ultrasonic targeting. MR thermometry revealed temperature elevations in the phantom reaching ablation levels, with clear evidence of greater heat accumulation within the tumor attributed to the effects of silica.

This phantom will serve as the main tool for evaluating the heating capabilities of the BRAINSONIC system and the feasibility of the proposed therapeutic approach of FUS ablation through 1-mm biocompatible skull inserts, as part of deliverable 5.2: MRI evaluation of the thermal heating. MR thermometry will be employed to assess whether adequately high temperatures are attained at the target and to evaluate any beam defocusing effects.

CONCLUSIONS

In conclusion, the proposed tumor-bearing brain/skull phantom, incorporating materials closely resembling human tissue properties, offers a realistic and cost-effective means for conducting preclinical MRgFUS ablation studies and testing relevant protocols. Importantly, the study outcomes validate its utility in exploring the suggested application of transcranial FUS ablation through removable 1-mm thick skull replicas. The temporary replacement of a small portion of the skull with a 1 mm skull replica is anticipated to facilitate the development of ablative temperatures within the tumor. This strategy leverages the benefits of single-element transducers, including cost-effectiveness and enhanced ergonomics, effectively addressing concerns related to insufficient ultrasonic penetration through the skull. While preliminary evidence is provided herein, further extensive experimentation utilizing the developed phantom will be conducted as part of Deliverable 5.2.

REFERENCES

[1] Béhin, A., Hoang-Xuan, K., Carpentier, A. F., & Delattre, J. (2003). Primary brain tumours in adults. The Lancet, 361(9354), 323–331. https://doi.org/10.1016/s0140-6736(03)12328-8.

[2] Grossman SA, Norris LK. (1995) Adjuvant and neoadjuvant treatment for primary brain tumors in adults. Semin Oncol. 22(6):530-9.

[3] Witthayanuwat, S., Pesee, M., Supaadirek, C., Supakalin, N., Thamronganantasakul, K., & Krusun, S. (2018). Survival analysis of glioblastoma multiforme. Asian Pac J Cancer Prev, 19(9), 2613–2617. https://doi.org/10.22034/apjcp.2018.19.9.2613.

[4] Gaillard F, Jones J, Layton B, et al. (2008) Glioblastoma, IDH-wildtype. Reference article, Radiopaedia.org (Accessed on 11 Mar 2024) https://doi.org/10.53347/rID-4910.

[5] Kim, Y., Lawler, S., Nowicki, M. O., Chiocca, E. A., & Friedman, A. (2009). A mathematical model for pattern formation of glioma cells outside the tumor spheroid core. Journal of Theoretical Biology, 260(3), 359–371. https://doi.org/10.1016/j.jtbi.2009.06.025.

[6] Chaddad, A., Desrosiers, C., Hassan, L., & Tanougast, C. (2016). A quantitative study of shape descriptors from glioblastoma multiforme phenotypes for predicting survival outcome. British Journal of Radiology, 89(1068), 20160575. https://doi.org/10.1259/bjr.20160575.

[7] Ulutin, C., Fayda, M., Aksu, G., Çetinayak, O., Kuzhan, O., Örs, F., & Beyzadeoğlu, M. (2006). Primary glioblastoma multiforme in younger patients: a single-institution experience. Tumori Journal, 92(5), 407–411. https://doi.org/10.1177/030089160609200507.

[8] Shukla, G., Alexander, G. S., Bakas, S., Nikam, R., Talekar, K., Palmer, J. D., & Shi, W. (2017). Advanced magnetic resonance imaging in glioblastoma: a review. Chinese Clinical Oncology, 6(4), 40. https://doi.org/10.21037/cco.2017.06.28.

[9] Agrawal, A. (2009). Butterfly glioma of the corpus callosum. Journal of Cancer Research and Therapeutics, 5(1), 43. https://doi.org/10.4103/0973-1482.48769.

[10] Kim, Y. J., Lee, D. H., Park, S. Y., & Kim, I. A. (2019). Optimal extent of resection for glioblastoma according to site, extension, and size: a population-based study in the temozolomide era. Neurosurgical Review, 42(4), 937–950. https://doi.org/10.1007/s10143-018-01071-3.

[11] Hansen, A., Desai, S., Cooper, A. N., et al. (2023). The clinical progression of patients with glioblastoma. Interdisciplinary Neurosurgery, 32, 101756. https://doi.org/10.1016/j.inat.2023.101756.

[12] Simpson, J. R., Horton, J., Scott, C., et al. (1993). Influence of location and extent of surgical resection on survival of patients with glioblastoma multiforme: Results of three consecutive radiation therapy oncology group (RTOG) clinical trials. International Journal of Radiation Oncology Biology Physics, 26(2), 239–244. https://doi.org/10.1016/0360-3016(93)90203-8.

[13] Sánchez-Herrera, F., Castro-Sierra, E., Gordillo-Domínguez, L. F., et al. (2009). Glioblastoma multiforme in children: experience at Hospital Infantil de Mexico Federico Gomez. Childs Nervous System, 25(5), 551–557. https://doi.org/10.1007/s00381-008-0780-8.

[14] Curtin, L., Whitmire, P., White, H., et al. (2021). Shape matters: morphological metrics of glioblastoma imaging abnormalities as biomarkers of prognosis. Scientific Reports, 11(1). https://doi.org/10.1038/s41598-021-02495-6.

[15] Thompson, L., & Campos, T. M. M. (2013). A head and neck simulator for radiology and radiotherapy. IEEE Transactions on Nuclear Science, 60(3), 1503–1511. https://doi.org/10.1109/tns.2013.2247063.

[16] Thompson, L., Dias, H. G., & Campos, T. M. M. (2013). Dosimetry in brain tumor phantom at 15 MV 3D conformal radiation therapy. Radiation Oncology, 8(1). https://doi.org/10.1186/1748-717x-8-168.

[17] Drakos T, Antoniou A, Evripidou N, Alecou T, Giannakou M, Menikou G, Constantinides G, Damianou C. (2021) Ultrasonic Attenuation of an Agar, Silicon Dioxide, and Evaporated Milk Gel Phantom. J Med Ultrasound, 29(4):239-249. doi: 10.4103/JMU.JMU_145_20.

[18] Antoniou A, Georgiou L, Christodoulou T, Panayiotou N, Ioannides C, Zamboglou N, Damianou C. (2022) MR relaxation times of agar-based tissue-mimicking phantoms. J Appl Clin Med Phys, 23(5):e13533. doi: 10.1002/acm2.13533.

[19] Guo J, Song X, Chen X, Xu M, Ming D. (2022) Mathematical Model of Ultrasound Attenuation With Skull Thickness for Transcranial-Focused Ultrasound. Front Neurosci, 15:778616. doi: 10.3389/fnins.2021.778616.